Simultaneous Multicomponent Topology Optimization using Unilateral Contact-Constraints

Timo Schmidt[1*] and Robert Seifried[1]

[1*]Institute of Mechanics and Ocean Engineering, Hamburg University of Technology, Eissendorfer Straße 42, Hamburg, 21073, Hamburg, Germany.

*Corresponding author(s). E-mail(s): timo.schmidt@tuhh.de;
Contributing authors: robert.seifried@tuhh.de;

Abstract

In this paper, a framework for topology optimization of assemblies considering unilateral contact-constraints is introduced. Here, an assembly consists of two or more components that are connected via joints, and the topology of all components of the assembly are optimized simultaneously. Therefore, linear-elastic material is considered and the augmented Lagrangian approach imposing Signorini's contact condition is used. In doing so, the unilateral characteristic of contact is taken into account. Furthermore, the influence of different contact modeling techniques, i.e. augmented Lagrangian approach, a standard penalty approach and a unilateral penalty approach, on the optimized designs are discussed. For topology optimization, the SIMP-approach is applied to all members of the assembly and sensitivity filtering is used. In consequence, the global design space of the optimization consists of the normalized densities of all members of the assembly. Using the proposed approach, one can optimize a topology for the whole assembly instead of optimizing all members of the assembly independently. This is of major importance, since changes in the topology of any member will lead to changes in the force transfer at the joints, which in consequence influences the optimization of all members of the assembly.

Keywords: Topology Optimization, simultaneous optimization, Multicomponent optimization, contact

1 Introduction

Topology optimization has been successfully applied to real world applications as well as many academic benchmarks. However, there are still limitations, because optimized designs are usually based on mechanical models and these models are limited by their assumptions. Especially in topology optimization, these assumptions should not significantly affect either the modeled mechanics or the optimization. This is a major challenge, as these models behave differently in optimization compared to mechanical analysis. Thus, assumptions that are often made in mechanical models might lead to poor performance in optimization. One example of such an often neglected phenomenon is the unilateral nature of contact in joints.

The necessity of modeling contact in Topology Optimization is demonstrated in several publications, i.e. [10, 23, 2, 16, 11, 7, 12, 19], where different aspects of contact-constrained topology optimization are discussed.
More precisely, the works of Fancello [10] and

Strömberg and Klarbring [23] deal with linear-elastic materials and unilateral boundary constraints. Here, a rigid contact obstacle is considered, and the contact is modeled using unilateral contact-conditions such as unilateral penalty approaches, augmented Lagrangian approaches to satisfy Signorini's Contact Conditions [22], as well as smooth approximations of Signorini's Contact Conditions. Luo et al. [16] introduces hyperelastic materials in contact-constrained Topology Optimization. Furthermore, Andrade-Campos et al. [2] uses a node-on-segment approach in topology optimization, to model the contact between two discretized domains.
Fernandez et al. [11] proposes the mortar segment-to-segment approach [17] for topology optimization, resulting in smooth contact forces and well-behaved convergence of the solution. In doing so, computing contact between multiple deformable bodies is possible, while the patch test is passed. The latter is not passed, if node-on-segment algorithms are used.
Internal contact and/or self-contact are addressed in Bluhm et al. [7] and Frederiksen et al. [12]. Here, the third medium contact approach of Wriggers et al. [26] is used in Topology Optimization. Similar results can be achieved using the numerical stabilization method of Scherz et al. [19]. In doing so, void and low-density elements are stabilized for geometrical nonlinear topology optimization.

Another challenging field is simultaneous multicomponent topology optimization. In contrast to standard topology optimization, in which each component of an assembly is optimized independent of its surrounding, simultaneous topology optimization minimizes an objective that is defined for the whole assembly. Thus, if the design of any component of the assembly changes, the design of others might adapt, since its loading path is effected by the design modification. Therefore, it is not possible to decompose the multicomponent optimization into several individual single component topology optimizations [8].

In the past, the following questions, among others, were examined in the context of assembly optimization. Where should the connections between the components be positioned? How many connection points are needed or how should the connection points be modeled? In this paper, the last questoin is addressed.
The other questions are addressed for example by Chickermane and Gea [8], who proposes a straight forward approach to optimize the topology of the components as well as the layout of the fasteners. Here, a grid of spring elements is introduced to transfer the loads from one to the other component. In doing so, two design domains are introduced, one for the material distribution and one for the interconnections. The latter is similar to the RAMP approach [6]. Several modifications and extensions have been made in order to tackle challenges such as continuous positioning of joints [25, 1].
However, for the modeling of the connections between two components generally either linear spring-like connections (see Chickermane and Gea [8] or Ambrozkiewicz and Kriegesmann [1]) or even rigid constraints are imposed (see Rakotondrainibe et al.[18]). Thus, the contact at the connecting joints is completely neglected in the assembly optimization process. This is particularly borderline, if bolt connections are considered. In consequence, the optimized designs are not optimized based on the actual loading paths at the connecting joints. This problem is either completely neglected or workarounds such as artificial non-design spaces are introduced.

This work extends the contact-constrained topology optimization framework by Strömberg and Klarbring [23] to handle simultaneous optimization of assemblies. In doing so, the influence of contact-constraints using both spring-like connections and actual unilateral contact conditions are investigated. It is shown, that the unilateral characteristic must not be neglected in topology optimization and that the augmented Lagrangian appraoch is superior.
The positions of the connecting joints are fixed and not part of the optimization, as the focus is on the unilateral contact behavior and its influence on the optimized assembly. Currently, only formulations based on linear spring models are developed to optimize the location of the joints simultaneously. These are not compatible with unilateral contact formulations, see Ambrozkiewicz and Kriegesmann for more details [1]. Future work should revisit the optimization of joint locations in combination with unilateral contact-constraints.
Next to multicomponent optimization, the presented method is also an extension to the single component optimization. Using the proposed method, external loads can also be applied at the

continuous contact structure, which is not possible using the framework of Strömberg and Klarbring [23] widening its applicability.

The article is organized as follows. In section 2, the equllibrium equations for the assembly - connected via unilateral contact constraints - are developed. Next in the section 3, the compliance optimization problem is formulated, and the adjoint method is used to compute the derivative of the objective efficiently. The optimization is performed to two different benchmark examples in section 4. Here also the influence of different contact laws in topology optimization is demonstrated. Last, conclusions are drawn in section 5.

2 Equilibrium equations of the contact problem

As basis for the latter defined topology optimization problem, the equilibrium equations are introduced. In Sec. 2.1, the equilibrium for the individual linear-elastic members of the assembly are derived. Next, the connecting joint constraints are introduced in Sec. 2.2, whereas the contact constraints are derived in Sec. 2.3. In the last Section 2.4, the results of the previous sections are combined and the global equilibrium equations are obtained. In doing so, the unilateral contact-constraints will be introduced to implicitly couple adjacent members of the assembly.

2.1 Linear-elastic equilibrium

The assembly consists of n_{Comp} components, and the equilibrium equations are based on the finite element analysis of each component j. Here for the topology optimization, a linear elastic constitutive law is considered and the modified SIMP approach [21] is applied. Hence, the Young's modulus E_i^j of the i-th finite element of the j-th component is a function of its normalized density $\varphi_i^j \in [0,1]$

$$E_i^j = E_{\min}^j + (\varphi_i^j)^p (E_{\max}^j - E_{\min}^j). \tag{1}$$

Thereby, φ_i^j are the design variables in the topology optimization and $\varphi_i^j = 0$ represents a void element, whereas $\varphi_i^j = 1$ represents an element filled with material. For the j-th member of the assembly, the Young's modulus of the void is

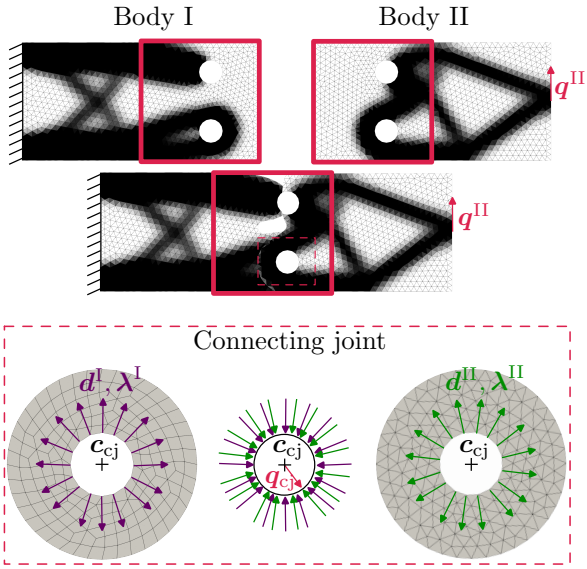

Fig. 1: Assembly connected via unilateral contact-constraints.

defined as $E_{\min}^j$ and the modulus of the material is $E_{\max}^j$. The penalization factor is set to $p = 3$. With the help of the physical Young's modulus E_i^j, one can assemble the stiffness matrix $\boldsymbol{K}^j = \boldsymbol{K}(\boldsymbol{\varphi}^j)$ of the j-th member of the assembly. Furthermore, the nodal displacement field $\boldsymbol{d}^j$, the nodal contact forces $\boldsymbol{f}_{\text{con}}^j$ and the external forces $\boldsymbol{q}^j$ acting at the j-th member of the assembly are introduced. Thus, the equilibrium equations for each member of the assembly read

$$\boldsymbol{K}(\boldsymbol{\varphi}^j)\boldsymbol{d}^j + \boldsymbol{f}_{\text{con}}^j - \boldsymbol{q}^j = \boldsymbol{0}. \tag{2}$$

Eq. (2) is amended by connecting joint constraints as well as contact conditions in order to compute the nodal contact forces $\boldsymbol{f}_{\text{con}}^j$.

2.2 Connecting joint constraint

The overall concept of connecting members of the assembly is visualized in Fig. 1, where an assembly of two components - namely body I and body II - is shown. Furthermore, an enlargement of the lower connecting joint is shown. The normal contact forces of body I are donated as $\boldsymbol{\lambda}^{\text{I}}$, whereas the normal contact forces of body II are donated as $\boldsymbol{\lambda}^{\text{II}}$. In order to transfer the occurring contact forces from body I to body II, a rigid continuous connecting joint is introduced. Note that the

following procedure is done for all n_{cj} connecting joints in the assembly.

The overall idea is, that the displacement of the connecting joint $\boldsymbol{c}_{\mathrm{cj}}^{k}$ is computed such that the sum of all contact forces $\boldsymbol{\lambda}^{\mathrm{I/II}}$ and possibly an additional external force acting on the joint $\boldsymbol{q}_{\mathrm{cj}}^{k}$ is zero. Thus, the equilibrium equation for the k-th connecting joint is based on the contact forces $\boldsymbol{\lambda}^{\mathrm{I/II}}$ of adjacent components and its external forces $\boldsymbol{q}_{\mathrm{cj}}^{k}$. Thus, this formulation allows applying loads directly at the connecting joint and the equilibrium equation is

$$\boldsymbol{\Gamma}^{k} = \sum_{A^{\mathrm{I}}=1}^{n_{\mathrm{con}}^{\mathrm{I}}} \left(\boldsymbol{n}_{A^{\mathrm{I}}}^{\mathrm{I}} \lambda_{A^{\mathrm{I}}}^{\mathrm{I}}\right) + \sum_{A^{\mathrm{II}}=1}^{n_{\mathrm{con}}^{\mathrm{II}}} \left(\boldsymbol{n}_{A^{\mathrm{II}}}^{\mathrm{II}} \lambda_{A^{\mathrm{II}}}^{\mathrm{II}}\right) + \boldsymbol{q}_{\mathrm{cj}}^{k} = \boldsymbol{0}, \tag{3}$$

where the number of nodes at the contact surface of the body I and II are $n_{\mathrm{con}}^{\mathrm{I/II}}$. In this formulation, the number of nodes at the contact surface of both components can be different. Therefore, the indices $A^{\mathrm{I/II}}$ are introduced. The contact force of a specific contact node A^{I} of body I is $\lambda_{A^{\mathrm{I}}}^{\mathrm{I}}$, whereas the A^{II}-th contact force of body II is $\lambda_{A^{\mathrm{II}}}^{\mathrm{II}}$. Note that the following computation of the normal direction must be performed for all nodes at the connecting joint of all adjacent components. For readability, the body index is dropped and only A is used.

The normal direction of A-th contact node $\boldsymbol{n}_{A}^{j}$ of the j-th component is shown in Fig. 2. The contact normal direction depends on the current nodal displacement $\boldsymbol{d}_{A}^{j}$ of the contact nodes, as

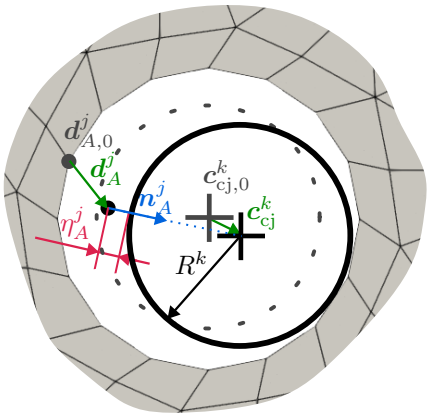

Fig. 2: Contact kinematics of the A-th contact node at the k-th connecting joint.

well as the joint's displacement $\boldsymbol{c}_{\mathrm{cj}}^{k}$. Hence, the normal direction of the A-th contact node is

$$\boldsymbol{n}_{A}^{j}(\boldsymbol{d}_{A}^{j}, \boldsymbol{c}_{\mathrm{cj}}) = \frac{(\boldsymbol{c}_{\mathrm{cj},0}^{k} + \boldsymbol{c}_{\mathrm{cj}}^{k}) - (\boldsymbol{d}_{A,0}^{j} + \boldsymbol{d}_{A}^{j})}{\|(\boldsymbol{c}_{\mathrm{cj},0} + \boldsymbol{c}_{\mathrm{cj}}) - (\boldsymbol{d}_{A,0}^{j} + \boldsymbol{d}_{A}^{j})\|}, \tag{4}$$

where the undeformed positions of the contact node $\boldsymbol{d}_{A,0}^{j}$ and the connection joint $\boldsymbol{c}_{\mathrm{cj},0}$ are introduced. If only small deformations of the contact nodes and the center of the connecting joint are observed, it is sufficient to approximate the normal direction. In consequence, the normal direction does only depend on the positioning in the undeformed configuration and is therefore constant. It reads

$$\boldsymbol{n}_{A}^{j} \approx \frac{\boldsymbol{c}_{\mathrm{cj},0}^{k} - \boldsymbol{d}_{A,0}^{j}}{\|\boldsymbol{c}_{\mathrm{cj},0}^{k} - \boldsymbol{d}_{A,0}^{j}\|}. \tag{5}$$

The normal directions are used to map the normal contact force vector $\boldsymbol{\lambda}^{j}$ into the nodal domain. The nodal contact forces introduced in Eq. (2) are

$$\boldsymbol{f}_{\mathrm{con}}^{j} = (\boldsymbol{N}^{j})^{\mathrm{T}} \boldsymbol{\lambda}^{j}, \tag{6}$$

where the mapping matrix $\boldsymbol{N}^{j}$ holds the normal directions. Having the equilibrium for the members of the assembly introduced in Eq. (2) and the connecting joint constraints of Eq. (3), the unilateral contact law must be added in order to finally solve the non-linear and non-smooth contact problem.

2.3 Contact condition

In order to compute the contact forces $\boldsymbol{\lambda}^{j}$ acting on each member of the assembly, it is necessary to distinguish between contact nodes, which are in contact and which are not in contact. Note that the contact conditions introduced in the following must be imposed for all adjacent members of the assembly. Looking at the example of Fig. 1, the contact conditions must be imposed connecting-joint wise for the contact nodes of body I and body II. This is done by introducing the contact gap η_{A}. Fig. 2 illustrates the deformed configuration of the A-th contact node at the connecting joint.

In doing so, the gap η_A can be computed as

$$\eta_A^j = (\boldsymbol{n}_A^j)^{\mathrm{T}} \left((\boldsymbol{c}_{\mathrm{cj},0}^k + \boldsymbol{c}_{\mathrm{cj}}^k) - (\boldsymbol{d}_{A,0}^j + \boldsymbol{d}_A^j) \right) - R^k, \tag{7}$$

where R^k is the radius of the connecting joint and $\boldsymbol{n}_A^j$ is the normal direction of Eq. (4). Eq. (7) can be rewritten as

$$\eta_A^j = (\boldsymbol{n}_A^j)^{\mathrm{T}} \left(\boldsymbol{g}_{A,0}^j + \boldsymbol{c}_{\mathrm{cj}}^k - \boldsymbol{d}_A^j \right) - R^k, \tag{8}$$

where the initial distance between the A-th contact node and the center of the k-th connecting joint is

$$\boldsymbol{g}_{A,0}^j = \boldsymbol{c}_{\mathrm{cj},0}^k - \boldsymbol{d}_{A,0}^j. \tag{9}$$

In order to link the contact gap η_A^j with the corresponding contact force λ_A^j, Signorini's contact conditions [22] are introduced, which read

$$\eta_A^j \geq 0, \quad \lambda_A^j \geq 0, \quad \eta_A^j \lambda_A^j = 0. \tag{10}$$

The third condition of Eq. (10) imposes, that if there is a gap $\eta_A^j > 0$ between the $A - th$ node and the connecting joint, no contact force is transmitted. Thus, the contact force must be $\lambda_A^j = 0$. Otherwise, the node is in contact with the connecting joint, meaning that the gap is $\eta_A^j = 0$ and therefore, a contact force $\lambda_A^j > 0$ is transmitted. For numerical implementations, Signorini's contact conditions can be imposed by non-smooth functions such as

$$\Phi_A^j = -\lambda_A^j + \max(0, \lambda_A^j - \eta_A^j) = 0. \tag{11}$$

Next, Eq. (8) is inserted into Eq. (11) yielding to

$$\Phi_A^j = -\lambda_A^j + \max \Bigg(0, \lambda_A^j + rR - r \left[(\boldsymbol{n}_A^j)^{\mathrm{T}} \left(\boldsymbol{g}_{A,0}^j + \boldsymbol{c}_{\mathrm{cj}}^k - \boldsymbol{d}_A^j \right) \right] \Bigg) = 0, \tag{12}$$

where $r > 0$ is a factor introduced to increase the numerical performance.

If different contact laws, such as the smoothing approaches of Facchinei et al. [9] or penalty contact laws [27], are used, only the contact function given by Eq. (12) is replaced, whereby the methodology remains the same. For contact-constrained topology optimization of a single component [23], it has been shown, that imposing Signorini's contact conditions in the strong form of Eq. (12) performs slightly better than the smoothing approach of Facchinei et al. [9]. The latter is therefore not examined further in this work.

The most commonly used contact models, are so-called penalty methods [27], where a penalty factor is introduced in order to penalize a deviation from the support. In almost all cases, this method neglects the one-sided characteristic of the contact. This both-sided contact laws have also been used in multicomponent topology optimization [8, 1]. In this case, the contact function is

$$\Phi_A^j = -\lambda_A^j - k\eta_A^j = 0, \tag{13}$$

where $k > 0$ is the penalty factor. Here, the both-sided penalty method is imposed using a Lagrange multiplier λ_A^j, which is rather unusual. This formulation is equivalent to the standard formulation. It is chosen to keep the structure of the global equilibrium equations unchanged, even if different contact models are used. The global equilibirum equations are introduced in section 2.4. If a unilateral characteristic of contact is taken into account, a unilateral penalty approach is used, its contact function reads

$$\Phi_A^j = -\lambda_A^j - \min(0, k\eta_A^j) = 0. \tag{14}$$

Note that a negative gap η_A^j is equivalent to a penetration. The unilateral penalty contact law has also been successfully applied in stress-constrained topology optimization [13].

2.4 Global equilibrium

In the following, the derivation focuses only on Signorini's contact conditions Eq. (12). If a penalty contact law is used, only the derivatives of the used contact law with respect to the state vector must be changed, which is straight forward for the penalty laws. More precisely, the Eqs. (22) to (24) must be adapted accordingly.

Combining the contact function Eq. (12) with the equilibrium Eq. (2) and the connecting joint constraints of Eq. (3) allows computing all displacements $\boldsymbol{d}^j$, all contact forces $\boldsymbol{\lambda}^j$ and the

displacements of all k connecting joints $\boldsymbol{c}_{\mathrm{cj}}^{k}$. Therefore, the overall set of equilibrium equations read

$$\boldsymbol{h}_{\mathrm{c}}(\boldsymbol{d},\boldsymbol{\lambda},\boldsymbol{c}_{\mathrm{cj}},\boldsymbol{\varphi}) = \begin{bmatrix} \left\{ \begin{matrix} \boldsymbol{K}(\boldsymbol{\varphi}^{j})\boldsymbol{d}^{j} + \boldsymbol{f}_{\mathrm{con}}(\boldsymbol{\lambda}^{j},\boldsymbol{c}) - \boldsymbol{q}^{j} \\ \boldsymbol{\Phi}^{j}(\boldsymbol{d}^{j},\boldsymbol{\lambda}^{j},\boldsymbol{c}_{\mathrm{cj}}) \end{matrix} \right\} \\ -\boldsymbol{\Gamma}^{k}(\boldsymbol{d},\boldsymbol{\lambda},\boldsymbol{c}_{\mathrm{cj}}^{k}) \end{bmatrix} = \boldsymbol{0}, \quad (15)$$

where the curly brackets must be formulated for each member of the assembly, whereas the connecting joint constraints $\boldsymbol{\Gamma}^{k}$ must be formulated for all connecting joints. In consequence, the unknown variables are the displacements $\boldsymbol{d}^{j}$ and contact forces $\boldsymbol{\lambda}^{j}$ of each component, as well as the deformation of the center positions of all connecting joints $\boldsymbol{c}_{\mathrm{cj}}$

$$\boldsymbol{x} = \begin{bmatrix} \begin{Bmatrix} \boldsymbol{d} \\ \boldsymbol{\lambda} \end{Bmatrix}^{j} \\ \boldsymbol{c}_{\mathrm{cj}} \end{bmatrix}. \quad (16)$$

This set of nonlinear and non-smooth equations (15) can be efficiently solved using a line-search algorithm. In order to apply a line-search algorithm, its linearization is needed. The linearization is derived for the example of Fig. 1 to make it as legibly as possible. Thus, the number of components and number of connecting joints is $n_{\mathrm{Comp}} = n_{\mathrm{cj}} = 2$. Furthermore, only small displacements are assumed and the normal directions are assumed to be constants. The resulting linearization is

$$\hat{\boldsymbol{h}}_{\mathrm{c}}(\boldsymbol{x},\boldsymbol{\varphi}) = \boldsymbol{J}_{\mathrm{c}}\boldsymbol{x} - \boldsymbol{r}_{\mathrm{c}} = \underbrace{\begin{bmatrix} \begin{Bmatrix} * & * \\ * & * \end{Bmatrix}^{\mathrm{I}} & \boldsymbol{0} & \begin{bmatrix} \boldsymbol{0} \\ \dfrac{\partial \boldsymbol{\Phi}^{\mathrm{I}}(\boldsymbol{x})}{\partial \boldsymbol{c}_{\mathrm{cj}}^{1}} \end{bmatrix} & \begin{bmatrix} \boldsymbol{0} \\ \dfrac{\partial \boldsymbol{\Phi}^{\mathrm{I}}(\boldsymbol{x})}{\partial \boldsymbol{c}_{\mathrm{cj}}^{2}} \end{bmatrix} \\ \boldsymbol{0} & \begin{Bmatrix} * & * \\ * & * \end{Bmatrix}^{\mathrm{II}} & \begin{bmatrix} \boldsymbol{0} \\ \dfrac{\partial \boldsymbol{\Phi}^{\mathrm{II}}(\boldsymbol{x})}{\partial \boldsymbol{c}_{\mathrm{cj}}^{1}} \end{bmatrix} & \begin{bmatrix} \boldsymbol{0} \\ \dfrac{\partial \boldsymbol{\Phi}^{\mathrm{II}}(\boldsymbol{x})}{\partial \boldsymbol{c}_{\mathrm{cj}}^{2}} \end{bmatrix} \\ \left\{ \boldsymbol{0} \ -\boldsymbol{n}_{A}^{\mathrm{I}} \right\}^{1} & \left\{ \boldsymbol{0} \ -\boldsymbol{n}_{A}^{\mathrm{II}} \right\}^{1} & \boldsymbol{0} & \boldsymbol{0} \\ \left\{ \boldsymbol{0} \ -\boldsymbol{n}_{A}^{\mathrm{I}} \right\}^{2} & \left\{ \boldsymbol{0} \ -\boldsymbol{n}_{A}^{\mathrm{II}} \right\}^{2} & \boldsymbol{0} & \boldsymbol{0} \end{bmatrix}}_{\boldsymbol{j}_{\mathrm{c}}}$$

$$\underbrace{\begin{bmatrix} \begin{Bmatrix} \boldsymbol{d} \\ \boldsymbol{\lambda} \end{Bmatrix}^{\mathrm{I}} \\ \begin{Bmatrix} \boldsymbol{d} \\ \boldsymbol{\lambda} \end{Bmatrix}^{\mathrm{II}} \\ \boldsymbol{c}_{\mathrm{cj}}^{1} \\ \boldsymbol{c}_{\mathrm{cj}}^{2} \end{bmatrix}}_{\boldsymbol{x}} - \underbrace{\begin{bmatrix} \begin{Bmatrix} \boldsymbol{q} \\ * \end{Bmatrix}^{\mathrm{I}} \\ \begin{Bmatrix} \boldsymbol{q} \\ * \end{Bmatrix}^{\mathrm{II}} \\ \boldsymbol{q}_{\mathrm{cj}}^{1} \\ \boldsymbol{q}_{\mathrm{cj}}^{2} \end{bmatrix}}_{\boldsymbol{r}_{\mathrm{c}}} = \boldsymbol{0}. \quad (17)$$

Here, the curly brackets are

$$\begin{Bmatrix} * & * \\ * & * \end{Bmatrix}^{j} = \begin{Bmatrix} \boldsymbol{K}(\boldsymbol{\varphi}^{j}) & (\boldsymbol{N}^{j})^{\mathrm{T}} \\ \dfrac{\partial \boldsymbol{\Phi}^{j}(\boldsymbol{x})}{\partial \boldsymbol{d}^{j}} & \dfrac{\partial \boldsymbol{\Phi}^{j}(\boldsymbol{x})}{\partial \boldsymbol{\lambda}^{j}} \end{Bmatrix}^{j}, \quad (18)$$

and

$$\begin{Bmatrix} \boldsymbol{q} \\ * \end{Bmatrix}^{j} = \left\{ \begin{matrix} \boldsymbol{q}^{j} \\ \underbrace{0}_{\text{no contact}} \end{matrix} , \underbrace{r\left((\boldsymbol{n}_{A}^{j})^{\mathrm{T}} \boldsymbol{g}_{A,0}^{j} - R^{j} \right)}_{\text{in contact}} \right\}. \quad (19)$$

If unilateral contact laws are imposed, the current state of all contact node must be checked. Using Signorini's contact condition, a node is in contact, if the argument of the max-function of the contact function Eq. (12) is active

$$\lambda_{A}^{j} - r\eta_{A}^{j} \geq 0. \quad (20)$$

If a unilateral penalty approach is used, the contact gap of Eq. (7) is used to determine the state of the contact node. Hence, a node is in contact, if the gap is

$$\eta_{A}^{j} \leq 0. \quad (21)$$

Last, the both-sided penalty contact law of Eq. (13) does not distinguish between nodes in contact and nodes that are not in contact.

Next, the partial derivatives of the contact laws from Eq. (17) and Eq. (18) are introduced. Note that the contact law Φ_{A}^{j} of the A-th contact node and j-th component does only depend on its nodal displacement $\boldsymbol{d}_{A}^{j}$, its contact force λ_{A}^{j}, as well as the center of the considered connecting

joint $\boldsymbol{c}^k$. The partial derivatives read

$$\frac{\partial \Phi_A^j(\boldsymbol{d}_A^j, \lambda_A^j, \boldsymbol{c}^k)}{\partial \boldsymbol{d}_A^j} = \begin{cases} \boldsymbol{0} & \text{, no contact} \\ r(\boldsymbol{n}_A^j)^{\mathrm{T}} & \text{, in contact} \end{cases}, \tag{22}$$

$$\frac{\partial \Phi_A^j(\boldsymbol{d}_A^j, \lambda_A^j, \boldsymbol{c}^k)}{\partial \lambda_A^j} = \begin{cases} -1 & \text{, no contact} \\ 0 & \text{, in contact} \end{cases}, \tag{23}$$

$$\frac{\partial \Phi_A^j(\boldsymbol{d}_A^j, \lambda_A^j, \boldsymbol{c}^k)}{\partial \boldsymbol{c}^k} = \begin{cases} 0 & \text{, no contact} \\ -r(\boldsymbol{n}_A^j)^{\mathrm{T}} & \text{, in contact} \end{cases}. \tag{24}$$

Finally, the non-linear equilibrium Eq. (15) and its linearization Eq. (17) are formulated. Given a density distribution $\tilde{\boldsymbol{\varphi}}$ of all members of the assembly and a guess for the state vector $\tilde{\boldsymbol{x}}$, a line-search algorithm is used to solve the non-linear equilibrium equations and therefore, compute the state vector $\boldsymbol{x}$. In this work, the default line-search Newton method of the PETSc library is used [4, 3, 5]. This technique employs cubic backtracking [15]. Even though a discontinuous contact problem is considered, the line-search is applied successfully. A line-search based approach is also applied in Strömberg and Klarbring [23]. The search direction of the line-search algorithm is

$$\boldsymbol{s} = \left(\boldsymbol{J}_{\mathrm{c}}\left(\tilde{\boldsymbol{x}}, \tilde{\boldsymbol{\varphi}}\right)\right)^{-1} \boldsymbol{h}(\tilde{\boldsymbol{x}}, \tilde{\boldsymbol{\varphi}}). \tag{25}$$

If not very small deformations are observed, the normal direction of the A-th contact node Eq. (4) is a function of the nodal displacement $\boldsymbol{d}_A^j$ and the center of the considered connecting joint $\boldsymbol{c}^k$. In consequence, the derivatives with respect $\boldsymbol{d}_A^j$ and $\boldsymbol{c}^k$ of the normal direction must be considered in Eq. (17) as well. In 2D problems, the derivatives of the normal direction are symmetric 2x2 matrices

$$\frac{\partial(\boldsymbol{n}_A^j)}{\partial(\boldsymbol{d}_A^j)} = \begin{bmatrix} -\dfrac{(\Delta_A^j)_2(\Delta_A^j)_2}{\|\boldsymbol{\Delta}_A^j\|^3} & \dfrac{(\Delta_A^j)_1(\Delta_A^j)_2}{\|\boldsymbol{\Delta}_A^j\|^3} \\ \dfrac{(\Delta_A^j)_1(\Delta_A^j)_2}{\|\boldsymbol{\Delta}_A^j\|^3} & -\dfrac{(\Delta_A^j)_1(\Delta_A^j)_1}{\|\boldsymbol{\Delta}_A^j\|^3} \end{bmatrix} \tag{26}$$

and

$$\frac{\partial(\boldsymbol{n}_A^j)}{\partial(\boldsymbol{c}^k)} = -\frac{\partial(\boldsymbol{n}_A^j)}{\partial(\boldsymbol{d}_A^j)}. \tag{27}$$

The vector $\boldsymbol{\Delta}_A^j$ in Eq. (26) and Eq. (27) is the vector between the deformed node A and the center of the connecting joint

$$\boldsymbol{\Delta}_A^j = (\boldsymbol{c}_{\mathrm{cj},0} + \boldsymbol{c}_{\mathrm{cj}}) - (\boldsymbol{d}_{A,0}^j + \boldsymbol{d}_A^j), \tag{28}$$

and $(\Delta_A^j)_{1/2}$ describe the first or second entry of the vector.
In 3D problems, the connecting joint has the form of a cylinder and its extrusion direction is $\boldsymbol{n}_{\mathrm{cj}}^k$. Therefore, the actual contact normal direction is obtained by projecting the cylinder surface onto a circle. In doing so, the contact nodes are free to deform tangential to the connecting joint. The resulting contact normal of the A-th contact node is

$$\left(\boldsymbol{n}_A^j(\boldsymbol{d}_A^j, \boldsymbol{c}_{\mathrm{cj}})\right)_{3\mathrm{D}} = \frac{(\boldsymbol{\Delta}_A^j) - (\boldsymbol{n}_{\mathrm{cj}}^k)^{\mathrm{T}}(\boldsymbol{\Delta}_A^j)\boldsymbol{n}_{\mathrm{cj}}^k}{\|(\boldsymbol{\Delta}_A^j) - (\boldsymbol{n}_{\mathrm{cj}}^k)^{\mathrm{T}}(\boldsymbol{\Delta}_A^j)\boldsymbol{n}_{\mathrm{cj}}^k\|}, \tag{29}$$

and the actual gap is

$$\left(\eta_A^j\right)_{3\mathrm{D}} = \left(\boldsymbol{n}_A^j\right)_{3\mathrm{D}}\left((**) - (\boldsymbol{n}_{\mathrm{cj}}^k)^{\mathrm{T}}(**)\boldsymbol{n}_{\mathrm{cj}}^k\right) - R. \tag{30}$$

The derivatives of the normal directions in 3D adapt accordingly.

3 Compliance optimization

In this work, the compliance of the assembly is minimized. The compliance consists of the compliance of each linear-elastic member of the assembly as well as the compliance of each joint. The latter results from external forces at the joints $\boldsymbol{q}_{\mathrm{cj}}^k$ and their center displacement. It reads

$$\begin{aligned} c &= \sum_{j=1}^{n_{\mathrm{Comp}}} (\boldsymbol{q}^j)^{\mathrm{T}} \boldsymbol{d}^j + \sum_{k=1}^{n_{\mathrm{cj}}} (\boldsymbol{q}_{\mathrm{cj}}^k)^{\mathrm{T}} \boldsymbol{c}_{\mathrm{cj}}^k \\ &= \begin{bmatrix} \{\boldsymbol{q}\} \\ \boldsymbol{0} \\ \boldsymbol{q}_{\mathrm{cj}} \end{bmatrix}^{j\,\mathrm{T}} \begin{bmatrix} \{\boldsymbol{d}\} \\ \boldsymbol{\lambda} \\ \boldsymbol{c}_{\mathrm{cj}} \end{bmatrix}^{j} = \boldsymbol{r}^{\mathrm{T}} \boldsymbol{x}, \end{aligned} \tag{31}$$

where $\boldsymbol{x}$ is the solution of the contact problem of Eq. (15). The design variables of the optimization are the normalized densities $\boldsymbol{\varphi}^j$ of all elements of all members. They are summarized in the global design vector

$$\boldsymbol{\varphi} = [\boldsymbol{\varphi}^1, \boldsymbol{\varphi}^2, \dots, \boldsymbol{\varphi}^{n_{\text{Comp}}}]^{\text{T}}. \tag{32}$$

Additionally, a volume constraint is imposed. One can either constrain the total volume of the assembly

$$g(\boldsymbol{\varphi}) = \sum_{j=1}^{n_{\text{Comp}}} \left(V(\boldsymbol{\varphi}^j)\right) - V_{\text{total}}, \tag{33}$$

or one constrains the volume of each member of the assembly individually

$$g^j(\boldsymbol{\varphi}) = V(\boldsymbol{\varphi}^j) - V_0^j, \tag{34}$$

where V_0^j is the maximum allowed volume for the j-th member of the assembly. The later results in n_{Comp} volume constraints. The resulting optimization problem reads

$$\begin{aligned} &\min_{\boldsymbol{\varphi}} \boldsymbol{r}^{\text{T}}\boldsymbol{x} \\ &\text{s.t.} \begin{cases} \boldsymbol{h}_{\text{c}}(\boldsymbol{\varphi}, \boldsymbol{x}) = \boldsymbol{0}, \\ g(\boldsymbol{\varphi}) \leq 0 \text{ or } g(\boldsymbol{\varphi}^j) \leq 0, \\ \boldsymbol{0} \leq \boldsymbol{\varphi}^j \leq \boldsymbol{1}. \end{cases} \end{aligned} \tag{35}$$

In doing so, one imposes either the global volume constraint of Eq. (33) or the local volume constraint of Eq. (34). Furthermore, the equilibrium equations of the contact problem $\boldsymbol{h}_{\text{c}}$ and the constraint on the design variables must be fulfilled. The optimization problem is solved using the method of moving asymptotes [24]. Therefore, the gradients with respect the design variables of the objective and the constraints are needed.

3.1 Gradient of the compliance

The gradient of the compliance of the assembly can be derived similarly to the single component contact-constraint topology optimization framework [23]. The compliance from Eq. (31) consists of the constant external forces vector $\boldsymbol{r}$ and the state vector $\boldsymbol{x}$. Thus, only the state vector $\boldsymbol{x}$ holding the displacements $\boldsymbol{d}^j$, the contact forces $\boldsymbol{\lambda}^j$ and the displacements of the connecting joints $\boldsymbol{c}_{\text{cj}}$ depends implicitly on the design variables. In order to compute the derivative of the state vector as efficient as possible, the adjoint vector $\boldsymbol{\zeta}$ is introduced. Then, the product of the adjoint vector and the linearized equilibrium equation (17) is subtracted from the compliance. The linearized equilibrium equations are zero for the solution of the contact problem, so that the adjoint vector can be chosen freely, if the solution of the contact problem is considered. The extended compliance is

$$\tilde{c}(\boldsymbol{x}) = \boldsymbol{r}^{\text{T}}\boldsymbol{x} - \boldsymbol{\zeta}^{\text{T}}\boldsymbol{h}_{\text{c}}(\boldsymbol{x}, \boldsymbol{\mu_z}). \tag{36}$$

In consequence, the gradient of the compliance with respect to the e-th entry of the global density vector $\boldsymbol{\varphi}$ is

$$\begin{aligned} \frac{\partial \tilde{c}(\boldsymbol{x})}{\partial \varphi_e} &= \frac{\partial \boldsymbol{r}}{\partial \varphi_e}^{\text{T}} \boldsymbol{x} + \boldsymbol{r}^{\text{T}} \frac{\partial \boldsymbol{x}}{\partial \varphi_e} - \boldsymbol{\zeta}^{\text{T}} \frac{\partial \boldsymbol{h}_{\text{c}}(\boldsymbol{x})}{\partial \varphi_e} \\ &= \boldsymbol{r}^{\text{T}} \frac{\partial \boldsymbol{x}}{\partial \varphi_e} - \boldsymbol{\zeta}^{\text{T}} \left[\frac{\partial \boldsymbol{J}_{\text{c}}(\boldsymbol{x})}{\partial \varphi_e} \boldsymbol{x} + \boldsymbol{J}_{\text{c}}(\boldsymbol{x}) \frac{\partial \boldsymbol{x}}{\partial \varphi_e} \right. \\ &\quad \left. - \frac{\partial \boldsymbol{r}_{\text{c}}}{\partial \varphi_e} \right] \\ &= \left[\boldsymbol{r}^{\text{T}} - \boldsymbol{\zeta}^{\text{T}} \boldsymbol{J}_{\text{c}}(\boldsymbol{x}) \right] \frac{\partial \boldsymbol{x}}{\partial \varphi_e} \\ &\quad - \tilde{\boldsymbol{\zeta}}^{\text{T}} \left[\frac{\partial \boldsymbol{J}_{\text{c}}(\boldsymbol{x})}{\partial \varphi_e} \boldsymbol{x} - \frac{\partial \boldsymbol{r}_{\text{c}}}{\partial \varphi_e} \right]. \end{aligned} \tag{37}$$

If the adjoint $\boldsymbol{\zeta}$ is chosen such that

$$\boldsymbol{r}^{\text{T}} - \boldsymbol{\zeta}^{\text{T}} \boldsymbol{J}_{\text{c}}(\boldsymbol{x}) = \boldsymbol{0}, \tag{38}$$

the costly derivative $\dfrac{\partial \boldsymbol{x}}{\partial \varphi_e}$ is eliminated. Hence, the gradient simplifies to

$$\frac{\partial c(\boldsymbol{x})}{\partial \varphi_e} = \frac{\partial \tilde{c}(\boldsymbol{x})}{\partial \varphi_e} = -\boldsymbol{\zeta}^{\text{T}} \left[\frac{\partial \boldsymbol{J}_{\text{c}}(\boldsymbol{x})}{\partial \varphi_e} \boldsymbol{x} - \frac{\partial \boldsymbol{r}_{\text{c}}}{\partial \varphi_e} \right]. \tag{39}$$

Furthermore, the vector $\boldsymbol{r}_{\text{c}}$ is independent of $\boldsymbol{\varphi}$, so that only the derivative of the Jacobian $\boldsymbol{J}_{\text{c}}$ with respect to $\boldsymbol{\varphi}$ must be computed. Coming from the single component framework of Strömberg and Klarbring [23], the derivative of the Jacobian is straight forward, since only the stiffness matrices $\boldsymbol{K}^j(\boldsymbol{\varphi}^j)$ of each member of the assembly depend explicitly on the design variables. Note that each

entry of the design vector $\boldsymbol{\varphi}$ describes the density of one finite element of one particular member of the assembly. In consequence, a member wise approach is very efficient, since all entries of the Jacobian, that are not related to the considered member of the assembly must be zero. In doing so, the global design vector $\boldsymbol{\varphi}$ is subdivided into the density vectors of each member $\boldsymbol{\varphi}^j$ and the gradient computation is done member by member. Following this approach, the gradient of the Jacobian is

$$\frac{\partial \boldsymbol{J}_{\mathrm{c}}(\boldsymbol{x})}{\partial \varphi_e^j} = \begin{Bmatrix} \dfrac{\partial \boldsymbol{K}(\boldsymbol{\varphi})}{\partial \varphi_e} & \mathbf{0} \\ \mathbf{0} & \mathbf{0} \end{Bmatrix}^j . \tag{40}$$

Here the derivative of the stiffness matrix with respect to the e-th element is the derivative of the e-th element's local stiffness matrix. In the derivative given by Eq. (40), the SIMP approach Eq. (1) must be considered. In summary, the derivative of the Jacobian of the single component implementation [23] must be done for each member of the assembly, in order to compute the gradient of the objective with respect to the design variables

$$\frac{\partial c(\boldsymbol{x})}{\partial \varphi_e} = \frac{\partial c(\boldsymbol{x})}{\partial \varphi_{\hat{e}}^j} = (\boldsymbol{\zeta}^j)^{\mathrm{T}} \begin{Bmatrix} \dfrac{\partial \boldsymbol{K}(\boldsymbol{\varphi}^j)}{\partial \varphi_{\hat{e}}^j} & \mathbf{0} \\ \mathbf{0} & \mathbf{0} \end{Bmatrix}^j \begin{Bmatrix} \boldsymbol{d} \\ \boldsymbol{\lambda} \end{Bmatrix}^j ,$$

where $\boldsymbol{\zeta}^j$ is the part of the adjoint vector corresponding to the nodal displacements and the contact forces of the j-th member. This member-wise concept is valid, since both the contact functions and the connecting joint constraints do not depend explicitly on the design variables.

3.2 Gradient of the volume constraints

Next to the objective, the gradients of the volume constraints are needed. The constraints are introduced in Eq. (33) and Eq. (34). If the total volume of the assembly is constrained, the derivative with respect to the density of the e-th element reads

$$\frac{\partial g(\boldsymbol{\varphi})}{\partial \varphi_e} = V_e, \tag{41}$$

where the volume of the e-th undeformed element is V_e. Otherwise, the volume of each member of the assembly is constrained. Thus, instead of only one volume constraint, n_{Comp} volume constraints are introduced. The gradient of each constraint is

$$\frac{\partial g^j(\boldsymbol{\varphi})}{\partial \varphi_e} = \begin{cases} V_{\hat{e}}^j & , \varphi_e \text{ is part of } j\text{-th component} \\ 0 & , \text{else} \end{cases} \tag{42}$$

For both volume constraints, the gradients with respect to the design variables are independent of the design variables and therefore constant.

4 Numerical Examples

The developed simultaneous multicomponent optimization framework is applied to 2D and 3D examples. First, the single component benchmark of Strömberg and Klarbring [23] is modified, in order to demonstrate the differences between forces that are applied to the structure or to the contact support structure. In this context, the influence of penalty contact conditions and Signorini's contact conditions is also investigated. Next, the L-beam example is analyzed for different two component designs, where the L-beam is modeled as assembly. At last, the 3D L-beam is considered to proof the scalability of the proposed method. All shown numerical examples are computed on a standard workstation.

4.1 2D benchmark of Strömberg and Klarbring

The benchmark example of Strömberg and Klarbring [23] and the resulting optimized design is shown in Fig. 3. In this benchmark, the connecting joint is considered as rigid contact support structure, which is fixed in space. The optimization is based on four load cases, where the applied load acts at the lower right corner of the design domain. The four load cases are $\boldsymbol{q}_1 = (1000\,\mathrm{N}, 0\,\mathrm{N})$, $\boldsymbol{q}_2 = (-1000\,\mathrm{N}, 0\,\mathrm{N})$, $\boldsymbol{q}_3 = (0\,\mathrm{N}, 1000\,\mathrm{N})$ and $\boldsymbol{q}_4 = (0\,\mathrm{N}, -1000\,\mathrm{N})$. In the implementation [20], the design domain is discretized by 4444 finite elements, resulting in 50 contact nodes at the rigid contact support. The considered linear-elastic material is characterized by a Poisson's ratio of 0.3 and a Young's modulus of 210 GPa. Further, the truncation radius of the used sensitivity filter [21] is 10 mm and the volume fraction

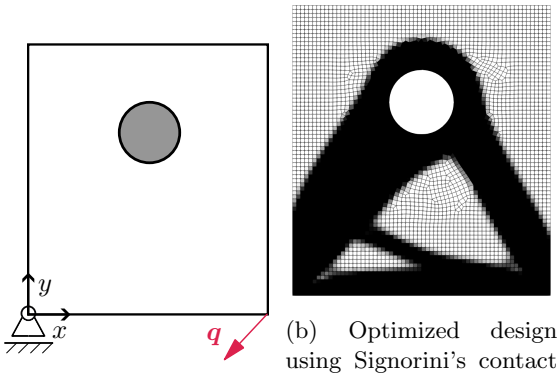

(a) Design space.

(b) Optimized design using Signorini's contact condition [20].

Fig. 3: Benchmark example of Strömberg and Klarbring[23] for unilateral contact constrained topology optimization.

is 0.5. A sensitivity filter is used, since the published results of Strömberg and Klarbring [23] are also based on this filter. However, other filtering techniques can be applied without any problems. The original benchmark does not consider adapting normal directions. Thus, the normal directions are considered to be constant and therefore only very small deformations are assumed. The normal directions are computed based on Eq. (5). All presented optimizations are terminated after 100 iterations.

The resulting compliance optimization problem of the original benchmark reads

$$\min_{\boldsymbol{\varphi}} \sum_{i=1}^{n=4} \left[\frac{1}{4} \left(\boldsymbol{q}_i^{\mathrm{T}} \boldsymbol{d}_i \right) \right] \quad \text{s.t.} \begin{cases} \boldsymbol{h}_{\mathrm{c}}(\boldsymbol{\varphi}, \boldsymbol{x})_i = \boldsymbol{0}, \\ V(\boldsymbol{\varphi}) - V_0 \leq 0, \\ \boldsymbol{0} \leq \boldsymbol{\varphi} \leq \boldsymbol{1}. \end{cases} \tag{43}$$

4.1.1 Modified benchmark using Signorini's contact condition

In contrast to the original benchmark of Strömberg and Klarbring[23], the proposed assembly optimization approach also allows applying forces at the connecting joint (contact support). Thus, a force transfer at the connecting joint is modeled, which therefore widens the applicability of contact-constrained topology optimization also for the single component optimization. Note that the very efficient framework for contact-constrained topology optimization of Strömberg and Klarbring[23] can be seen as sub-problem of the proposed method, where the connecting joint cannot move. In doing so, the connecting joint constraint of Eq. (3) is replaced by

$$\boldsymbol{\Gamma}^k = \boldsymbol{c}_{\mathrm{cj}}^k = \boldsymbol{0}. \tag{44}$$

The modified benchmark for the proposed method is shown in Fig. 4a. The same load cases are considered as in the original benchmark. However, they are now applied at the connecting joint instead of the lower right corner of the design domain. This is possible, since the center of the connecting joint is not fixed in space anymore. As in the original benchmark, Signorini's contact condition is used. Note that the modified as well as the initial Benchmark are not symmetric, so that non-symmetric optimized designs are expected and observed. The resulting optimization problem is now

$$\min_{\boldsymbol{\varphi}} \sum_{i=1}^{n=4} \left[\frac{1}{4} \left(\boldsymbol{r}_i \boldsymbol{x}_i \right) \right] \quad \text{s.t.} \begin{cases} \boldsymbol{h}_{\mathrm{c}}(\boldsymbol{\varphi}, \boldsymbol{x})_i = \boldsymbol{0}, \\ V(\boldsymbol{\varphi}) - V_0 \leq 0, \\ \boldsymbol{0} \leq \boldsymbol{\varphi} \leq \boldsymbol{1}. \end{cases} \tag{45}$$

The obtained design using Signorini's contact condition is shown in Fig. 4b. Next to this, the convergence plots of the original benchmark as

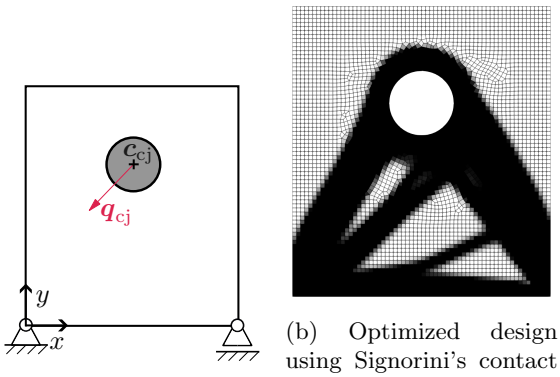

(a) Design space.

(b) Optimized design using Signorini's contact condition.

Fig. 4: Modified benchmark example using the multicomponent method.

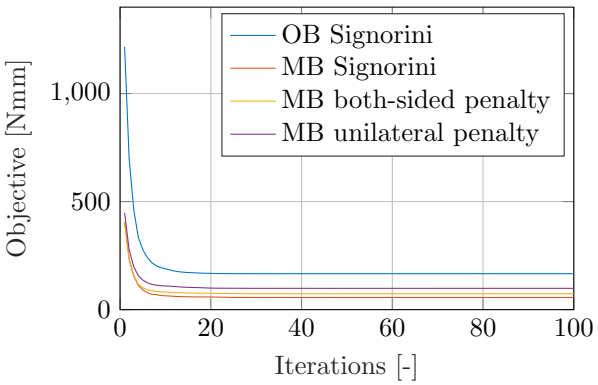

Fig. 5: Convergence of the performed optimizations of Fig. 3, Fig. 4 and 6. (OB - Original Benchmark, MB - Modified Benchmark)

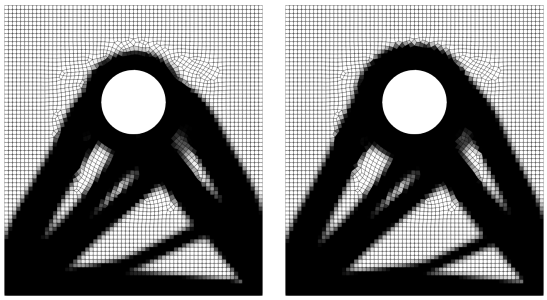

(a) Assembly opt. using both-sided penalty contact law.

(b) Assembly opt. using unilateral penalty contact law.

Fig. 6: Comparison of the optimized designs using penalty contact laws, where forces are applied at the connecting joints.

well as the modified setup are shown in Fig. 5 and both methods converge as expected.

Taking a closer look at Fig. 3b and Fig. 4b reveals, that the optimized design adapts to the modifications of the setup. Hence, it is crucial to differentiate between the existing contact-constrained topology optimization framework of Strömberg and Klarbring[23] and the proposed method of this work also for the single component optimization.

4.1.2 Modified benchmark using penalty approaches

In topology optimization as well as finite element analysis, contact is often modeled using penalty approaches. This is still nowadays the most common modeling approach, if contact is considered, and therefore, also successfully applied in the assembly optimization approaches of (see e.g. Chickermane and Gea[8], Thomas et al[25] or Ambrozkiewicz and Kriegesmann[1]). Especially in assembly optimization, it has the advantage that the locations of the connecting joints can be optimized easily, since the both-sided penalty contact law does not add any non-linearity to the problem and the unilateral characteristic of contact is neglected. However, the influence of penalty approaches on the final design is not often discussed. Therefore, the influence is investigated using the modified benchmark of Fig. 4. The penalty factor is set to $k = 2000\,\mathrm{N/mm}$ for the both-sided and unilateral contact law.

The resulting optimized designs are visualized in Fig. 6 and the convergence history of both optimization is added to Fig. 5. The optimized design using the standard both-sided penalty approach is shown in Fig. 6a. If this design is compared to Fig. 4b (using Signorini), major differences are observed. In particular, significantly less material is provided in the vicinity of the contact structure and some struts are split. Comparing the final design using the unilateral penalty approach (see Fig. 6b) to the both-sided penalty design (see Fig. 6a), significantly more material is distributed in the vicinity of the contact structure, while the struts are very similar. Nonetheless, the strut appearance is still very different in comparison to the design computed with Signorini's contact conditions (see Fig. 4b).

Furthermore, the compliance is reduced the most for the design using the Signorini's contact condition. This is shown in Table 1, where the three final designs of the modified benchmark are evaluated twice. Once, it is evaluated using the

Table 1: Evaluation of the optimized designs from Fig. 4 and Fig. 6 based on the used contact law and Signorini's contact conditions.

final design	Compl. in opt.	Compl. using Signorini
Signorini Fig. 4b	56.13	56.13
both-sided pen. Fig. 6a	73.79	58.22
unilateral pen. Fig. 6b	98.62	56.96

contact law used in optimization and once using Signorini's contact condition for comparision. In comparison to the design of Fig. 4b, the performance of the design computed with the both-sided contact law is 3.7% worse. Thus, using both-sided penalty contact laws in topology optimizations results in different designs with noticeable losses in performance. Further, the performance of the design based on the unilateral contact law is a lot better. Nonetheless, the design is still 1.5% off compared to the design using Signorini's contact condition. However, during optimization, the compliance is highest with the unilateral penalty approach. This is expected because, unlike the two-sided approach, only pressure regions transmit contact forces, leading to more penetration at the contact support. In consequence, a higher compliance is observed, if the penalty factor is the same for both penalty methods.

These results imply that it is crucial to consider the unilateral characteristic of contact in topology optimization, in order to obtain good performing final designs. Note that one could also increase the penalty factor k in order to obtain better results for the penalty approaches, but the Jacobian (see Eq. (17)) will become more and more ill posted and the computation time will increase significantly. In this example, the whole optimization using the both-sided penalty method took 501 s, whereas the unilateral penalty optimization took 505 s. The optimization approach using Signorini's contact condition takes approximately 4 times longer. Consequentially, the unilateral penalty approach comes at zero extra costs, in comparison to the both-sided penalty approach, whereas Signorini's contact condition is the most expensive, while having the best performing design.

4.1.3 Adapting normal direction

Until now, very small deformations were assumed, so that the normal direction of each contact node is not updated and therefore constant. Here, the modified benchmark is optimized using Signorini's contact condition and changes of the contact normal direction are considered. Thus, Eq. (4) is used to update the normal direction while solving the global equilibrium equations. The final design is shown in Fig. 7 and only minor differences to the design of Fig. 4b are observed. Thus, assuming small deformations is reasonable for this example.

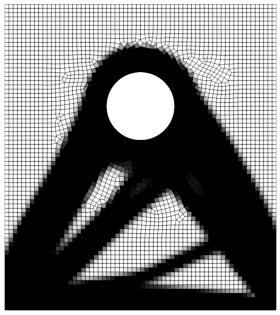

Fig. 7: Modified benchmark with adapting contact normal directions.

4.2 2D L-beam example

The considered L-beam example is visualized in Fig. 8. There, the design space as well as the single component optimized design without using contact are shown. The dimensions of the design space and boundary conditions are based on Holmberg et al. [14]. The material parameters are unchanged to Sec. 4.1, while the truncation radius of the sensitivity filter is set to 3.5. Dirichlet boundary conditions are imposed at the top and a vertical load of $\boldsymbol{q} = (0, -1500\,\mathrm{N})^{\mathrm{T}}$ is applied at the top of the tip. The volume fraction is set to 0.5.

4.2.1 Multicomponent optimization using Signorini's contact condition

In the following, the L-beam is optimized using the proposed multicomponent optimization approach.

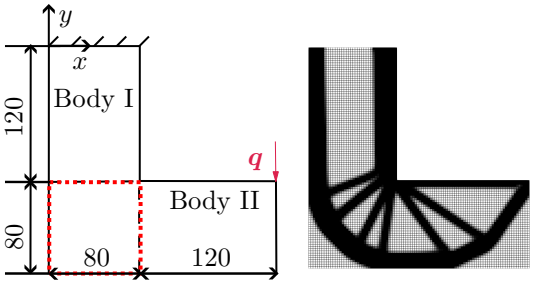

(a) Multicomponent design space. (b) Single component opt. design.

Fig. 8: Design space and single component reference for the L-Beam.

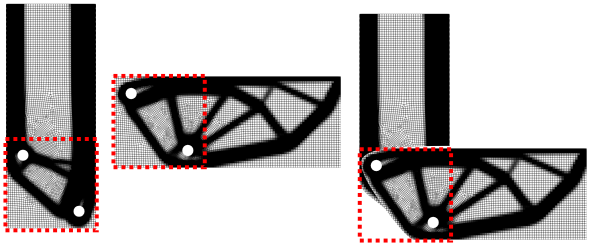

(a) 2 connecting joints assembly.

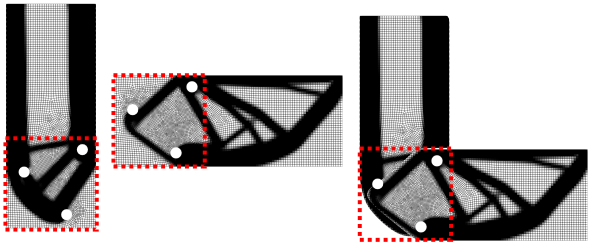

(b) 3 connecting joints assembly.

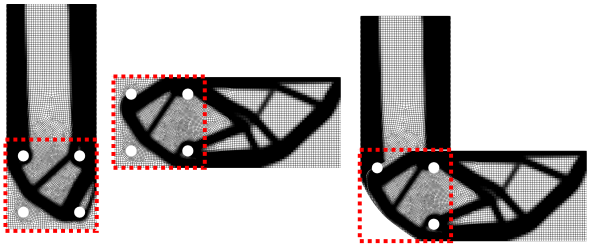

(c) 4 connecting joints assembly.

Fig. 9: Optimized designs of the L-beam using Signorini's contact condition.

Therefore, the L-beam is decomposed into two beam-like components forming the assembly. In doing so, the red area of Fig. 8a is the overlap of both components of the assembly. This is where connecting joints can be placed. The radius of each connecting joint is set to 5 mm. Here, three different setups with a different number of connecting joints are investigated and a global volume constraint with a volume fraction of 0.5 is imposed.

The obtained optimized designs are shown in Fig. 9 and the convergence plots of all optimized designs are shown in Fig. 10. It is worth mentioning, that the final compliance of the single component design (Fig. 8b) is the lowest. However, the design with 3 joints (Fig. 9b) and the 4 joint design (Fig. 9c) are close by. More precisely, the compliance of the final design of

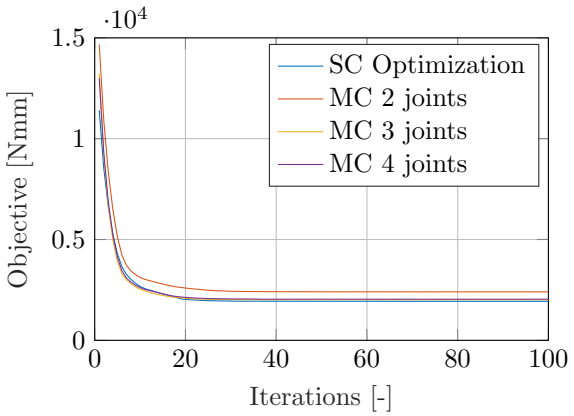

Fig. 10: Convergence of the optimizations of the L-beam of Fig. 9. (SC - single component, MC - Multicomponent)

the single component compliance optimization is 1935.0 Nmm, whereas the compliance of the 3 joint design is 2013.6 Nmm and the 4 joint design has a final compliance of 2040.3 Nmm. Only the design with 2 connecting joints performs significantly worse, with a final compliance of 2403.2 Nmm. This shows, that the number of joints as well as their positioning is challenging [1]. However, very good performance is observed, if the joints are placed inside struts of the standard single component compliance optimization results of Fig. 8b. In this example, this is done for the 3 joint design, which is the best performing assembly.

Another noteworthy observation is the unused fourth contact support in Fig. 9c. All calculated contact forces at this support are about the same size as the relative tolerance of the convergence criteria used by the line-search algorithm solving the contact problem. The relative tolerance is set to $r_{\text{tol}} = 10^{-8}$. Thus, no forces are transmitted at this joint. In these examples, the unilateral characteristic of contact is considered, so that the optimization algorithm has no interests in placing material outside the pressure zones of the joints. This can be seen at any joint of Fig. 9a to Fig. 9c. As for the unused joint of Fig. 9c, the contact forces of contact nodes that belong to void elements are always in the order of magnitude of the relative tolerance. Hence, forces are only transmitted at contact nodes of filled finite elements.

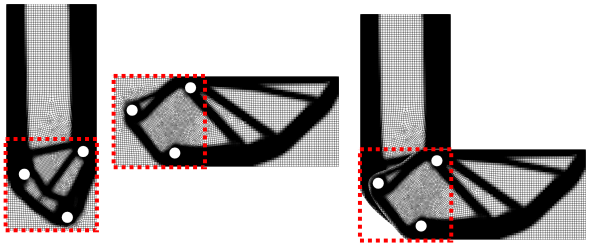

(a) 3 connecting joints assembly both-sided penalty.

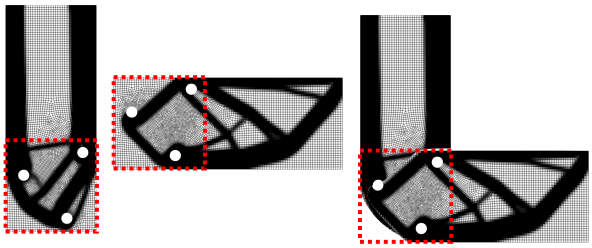

(b) 3 connecting joints assembly unilateral penalty.

Fig. 11: Optimized designs of the L-beam using penalty contact laws.

4.2.2 Multicomponent optimization using penalty approaches

The 3 joint design is also optimized using the both-sided penalty and unilateral penalty approach. In these examples, the penalty factor is set again to $k = 2000\,\mathrm{N/mm}$. The obtained optimized designs are shown in Fig. 11. As in the former section 4.1, the both-sided penalty design results in a different design with a poorer performance, whereas considering the unilateral penalty law results in an overall similar design to Fig. 9b. Comparing the design using the unilateral penalty law (see Fig. 11b) and Signorini's contact condition (see Fig. 9b), differences around the connecting joints are observed at the vertical component (body I), whereas the struts differ in size significantly at the horizontal member (body II) of the assembly. A closer look at the upper right joint of the horizontal component of Fig. 11a demonstrates the impact of neglecting the unilateral characteristic perfectly. In contrast to the unilateral designs, the diagonal struts do not go around this connecting joint, so that only tensile forces are transmitted. Thus, these struts are dysfunctional in practice.

Furthermore, it is worth mentioning that once again the computation time of both penalty methods is very similar, while using Signorini's contact condition is only 3 times slower. However, this changes drastically, if the four joint design is computed. If the both-sided penalty model is used, the line search algorithm suddenly needs a lot more iterations. In consequence, the numerical costs increase tremendously and exceed by magnitudes the costs of the unilateral penalty law and Signorini's contact condition.

A closer look reveals that the progress of the line search algorithm shrinks drastically compared to the other two contact laws. In consequence, no optimization can be performed in reasonable time using the both-sided contact law under these conditions.

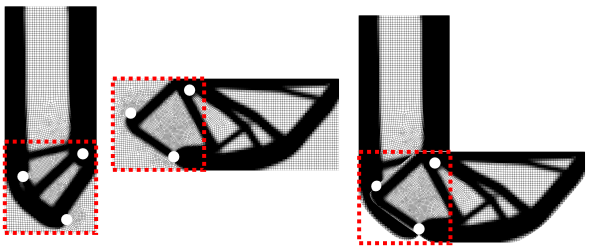

(a) Signorini's contact condition.

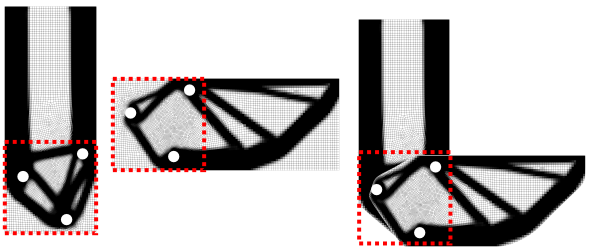

(b) Both-sided penalty.

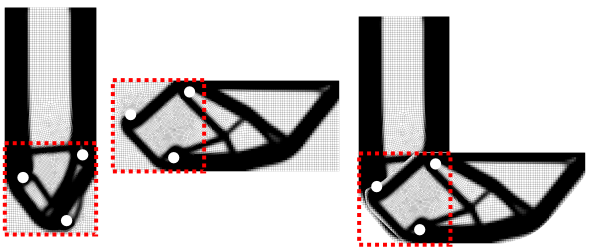

(c) Unilateral penalty.

Fig. 12: L-beam with adapting contact normal directions.

4.2.3 Adapting normal direction

The former L-beam optimizations are performed assuming small displacements, so that the contact normal directions can be approximated using Eq. (5). This assumption is removed and therefore, Eq. (4) is used to compute the normal directions. Thus in this section, each contact normal direction depends on the nodal displacement of the contact node as well as the displacement of the center of the connection joint. The optimized designs are shown in Fig. 12 and major differences are observed, in comparison to the solution assuming small displacements of Fig. 9b and Fig. 11.

Taking a closer look at the results imposing Signorini's contact conditions, the vertical component (body I) of Fig. 9b and Fig. 12a are almost identical, while the horizontal component (body II) differs significantly inside the red box. The struts differ in size and more importantly, the strut at the lower connecting joint have a complete different angle of attack. This happens, because the loading path inside the components changes, if the adapting normal directions are considered. In consequence, the optimized design adapts.

One has to admit, that the design at the lower connecting joint of the horizontal component might fail in practice, since the struts might slip from the connecting joint. However, this can be easily solved by introducing a non-design space around the connecting joint, which is common practice in multicomponent optimization [1]. Using Signorini's contact condition, the width of the non-design space is actually known, since the actual characteristic of contact mechanics are considered and therefore, the actual loading path inside the component is taken into account during optimization. In consequence, the width of the non-design space depends exclusively on the manufacturing constraints of the used fasteners. Using penalty contact laws, this assumptions hold only if extremely high penalty factors are used, since the absolute value of the penalty factor and the unilateral characteristic influence the loading path and therefore, the optimized design.

The optimized design based on penalty contact laws ($k = 2000\,\mathrm{N/mm}$) are shown in Fig. 12b and Fig. 12c. Also here, the optimized design considering the adapting contact normal direction differ significantly from the previous designs assuming very small displacements of Fig. 11. If the both-sided penalty approach is used, the final design once again includes dysfunctional struts at the upper two connecting joints (see Fig. 12b). Here, the struts of the horizontal component transmit tension forces, which is nonphysical in the context of contact. Once again, one can introduce non-design spaces to overcome this problem. However using both-sided penalty approach, the width of the non-design spaces is not only constraint by the manufacturing constraints of the fasteners. The underlying model transmits tension forces at the joints. Consequentially, the underlying model will underestimate the needed material at the joints, which might lead to failure in practice. Thus, the width of the non-design space must be chosen very conservatively, which in turn has a significant impact on the performance of the optimized design.

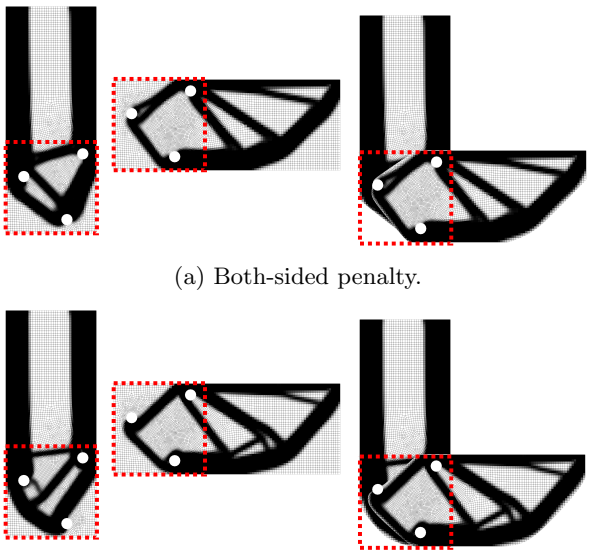

(a) Both-sided penalty.

(b) Unilateral penalty.

Fig. 13: L-beam with adapting contact normal directions and increased penalty factor $k = 10000\,\mathrm{N/mm}$.

In Fig. 13, the penalty factor is increased to $k = 10000\,\mathrm{N/mm}$, in order to show the impact of the penalty factor of the both-sided and unilateral contact law. In doing so, the optimized design should become more and more similar to the design obtained by Signorini's contact condition (see Fig. 12a). Especially, the unilateral

design transforms towards the design using Signorini's contact condition. However, especially the appearance of the struts between the lower and left connection joint is still very different. At the same time, the computation times increase significantly for both penalty. Now, the both-sided penalty law is four times slower, than the optimizations using Signorini's contact condition and the unilateral penalty law is two times slower, than using Signorini's contact condition. Furthermore, its worth mentioning, that considering adapting contact normal directions reduces the computation time by 20%, if Signorini's contact conditions are imposed, while the computation times of both penalty methods increase in comparison to the constant contact normal directions.

4.3 3D L-beam example

The presented simultaneous optimization approach is also applied to a 3D example of the L-beam. Therefore, the 3 joint design space is extruded into z-direction and the two components are placed next to eachother. The vertical beam is hold in place at it's four upper corners and a load is distributed along the tip of the beam. Furthermore, symmetry is imposed so that the connecting joints cannot move along the z-axis. In doing so, a total of 242534 finite elements are considered, and each component has 1056 contact nodes. The results are shown in Fig. 14 and Fig. 15. The contact is modeled using Signorini's contact conditions. Thus, no penalty approach is used here.

The overall appearance of the vertical component of the 3D design is similar to the 2D design of Fig. 9b. However, there is also material distributed around the lower connecting joint and some differences are observed at the top. In contrast to the vertical component, the horizontal component differs significantly from the 2D design. Less struts are used and a 'I-profile' like structure is found. Hereby, the width of the inner support differs over the height of the component. Interestingly, the appearance close to the connecting joint is similar to the 2D design. Due to the applied symmetry constraint, the actual appearance of the optimized assembly is shown in Fig. 15.

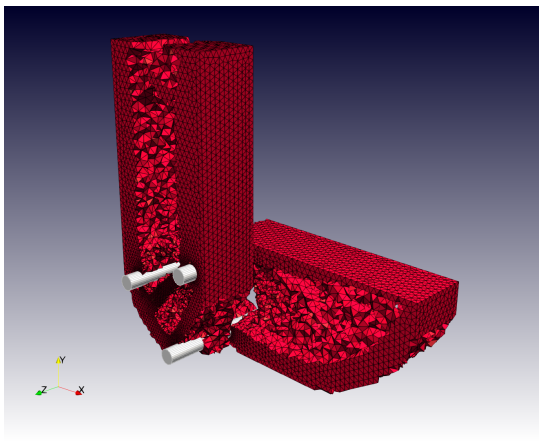

(a) Frontside.

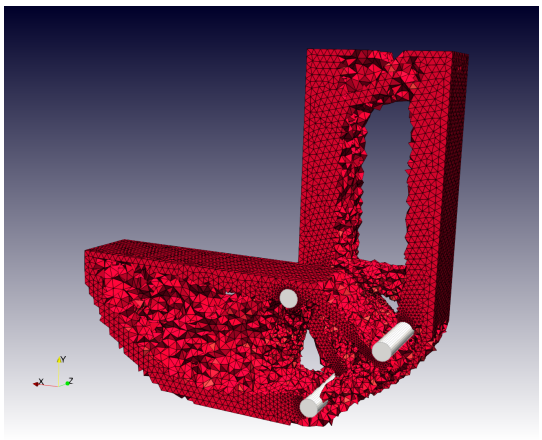

(b) Backside.

Fig. 14: Optimized design of the L-Beam using Signorini's contact condition.

5 Conclusion

In this paper, the general framework for contact-constrained topology optimization of linear-elastic structures of Strömberg and Klarbring [23] is extended to simultaneous optimization of assemblies. Furthermore, external loads can be applied at the connecting joints extending the single component framework of Strömberg and Klarbring [23] significantly. In doing so, different benchmark examples are shown and the necessity of modeling the unilateral characteristic of contact in optimization is demonstrated.

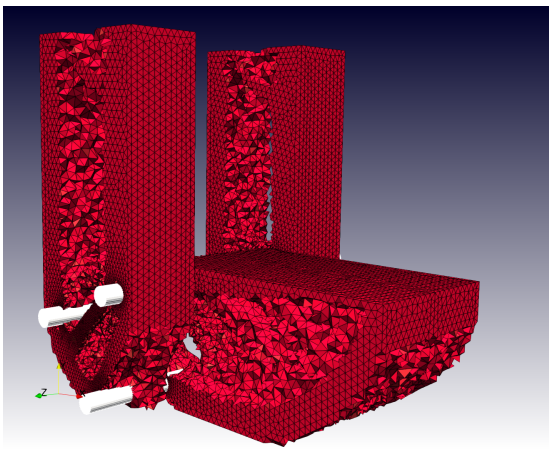

Fig. 15: Final design including the symmetry.

It is shown, that neglecting the unilateral characteristic in optimization, e.g. using the both-sided penalty approach, results in poorer performing optimized design. One might argue, that one will always introduce a non-design space around the entire connecting joint. Nevertheless, unilateral contact laws must be considered, as otherwise both the compression and tension zones of the contact surface contribute to the stiffness of the joint. The optimizer will take advantage of this non-physical assumption, which in practice can lead to dysfunctional joints.
When considering the unilateral characteristic, the actual contact mechanics are taken into account during the optimization. In consequence, topology optimization will place a sufficient amount of material in the pressure zones at the contact surface. Therefore, a non-design space around a connecting joint is only limited by manufacturing constraints, like the necessary support for fasteners (e.g., bolt connections). The size of these non-design spaces is known in advance.

Furthermore, the augmented Lagrangian approach directly satisfying Signorini's contact-conditions is compared to the unilateral penalty approach. Here, the penalty approach was sufficient, for the single component example, while in the multicomponent simulations, the computation time of the penalty approaches exceeded the computation time using the augmented Lagrangian approach significantly. Therefore, the augmented Lagrangian approach is recommended, since it is easier to handle in practice.

As stated in the introduction, future work should also focus on optimizing the placement of the connecting joints. Here new coupling techniques must be developed, as the state of the art methods are not applicable using unilateral contact constraints.
Furthermore, segment-to-segment contact formulations should be investigated, especially if stress-constrained topology optimization is of interest. In contrast to the node-on-segment approaches, the approach of Fernandez et. al. [11] results in a smoother contact pressure and passes the patch test.

Declarations

Funding. The current work is a part of the research training group "Simulation-Based Design Optimization of Dynamic Systems Under Uncertainties" (SENSUS) funded by the state of Hamburg within the Landesforschungsförderung under project number LFF-GK11.

Conflict of interest. On behalf of all authors, the corresponding author states that there is no conflict of interest.

Replication of results. The used in-house Toolbox TOptiMuM cannot be published at this time. Nonetheless, all needed parameters to recompute the results are mentioned in the work.

References

[1] Olaf Ambrozkiewicz and Benedikt Kriegesmann. Simultaneous topology and fastener layout optimization of assemblies considering joint failure. *International Journal for Numerical Methods in Engineering*, 122:294–319, 1 2021.

[2] António Andrade-Campos, António Ramos, and José A. Simões. A model of bone adaptation as a topology optimization process with contact. *Journal of Biomedical Science and Engineering*, 05:229–244, 2012.

[3] Satish Balay, Shrirang Abhyankar, Mark F. Adams, Steven Benson, Jed Brown, Peter Brune, Kris Buschelman, Emil Constantinescu, Lisandro Dalcin, Alp Dener, Victor Eijkhout, Jacob Faibussowitsch, William D. Gropp, Václav Hapla, Tobin Isaac, Pierre Jolivet, Dmitry Karpeev, Dinesh Kaushik,

Matthew G. Knepley, Fande Kong, Scott Kruger, Dave A. May, Lois Curfman McInnes, Richard Tran Mills, Lawrence Mitchell, Todd Munson, Jose E. Roman, Karl Rupp, Patrick Sanan, Jason Sarich, Barry F. Smith, Stefano Zampini, Hong Zhang, Hong Zhang, and Junchao Zhang. PETSc/TAO users manual. Technical Report ANL-21/39 - Revision 3.21, Argonne National Laboratory, 2024.

[4] Satish Balay, Shrirang Abhyankar, Mark F. Adams, Steven Benson, Jed Brown, Peter Brune, Kris Buschelman, Emil M. Constantinescu, Lisandro Dalcin, Alp Dener, Victor Eijkhout, Jacob Faibussowitsch, William D. Gropp, Václav Hapla, Tobin Isaac, Pierre Jolivet, Dmitry Karpeev, Dinesh Kaushik, Matthew G. Knepley, Fande Kong, Scott Kruger, Dave A. May, Lois Curfman McInnes, Richard Tran Mills, Lawrence Mitchell, Todd Munson, Jose E. Roman, Karl Rupp, Patrick Sanan, Jason Sarich, Barry F. Smith, Stefano Zampini, Hong Zhang, Hong Zhang, and Junchao Zhang. PETSc Web page. https://petsc.org/, 2024.

[5] Satish Balay, William D. Gropp, Lois Curfman McInnes, and Barry F. Smith. Efficient management of parallelism in object oriented numerical software libraries. In E. Arge, A. M. Bruaset, and H. P. Langtangen, editors, *Modern Software Tools in Scientific Computing*, pages 163–202. Birkhäuser Press, 1997.

[6] Martin P. Bendsøe and Ole Sigmund. *Topology Optimization: Theory, Methods and Applications*. Springer Science and Business Media, Berlin, Heidelberg, 2 edition, 2013.

[7] Gore Lukas Bluhm, Ole Sigmund, and Konstantinos Poulios. Internal contact modeling for finite strain topology optimization. *Computational Mechanics*, 67:1099–1114, 4 2021.

[8] H. Chickermane and H. C. Gea. Design of multi-component structural systems for optimal layout topology and joint locations. *Engineering with Computers*, 13:235–243, 12 1997.

[9] F. Facchinei, H. Jiang, and L. Qi. A smoothing method for mathematical programs with equilibrium constraints. *Mathematical Programming*, 85:107–134, 1999.

[10] E A Fancello. Topology optimization for minimum mass design considering local failure constraints and contact boundary conditions. 32:229–240, 2006.

[11] Felipe Fernandez, Michael A. Puso, Jerome Solberg, and Daniel A. Tortorelli. Topology optimization of multiple deformable bodies in contact with large deformations. *Computer Methods in Applied Mechanics and Engineering*, 371:113288, 11 2020.

[12] Andreas Henrik Frederiksen, Ole Sigmund, and Konstantinos Poulios. Topology optimization of self-contacting structures. *Computational Mechanics*, 73:967–981, 4 2024.

[13] Yongsheng Han, Bin Xu, Zunyi Duan, and Xiaodong Huang. Stress-based topology optimization of continuum structures for the elastic contact problems with friction. *Structural and Multidisciplinary Optimization*, 65(2):54, feb 2022.

[14] Erik Holmberg, Bo Torstenfelt, and Anders Klarbring. Stress constrained topology optimization. *Structural and Multidisciplinary Optimization*, 48(1):33–47, jul 2013.

[15] J. E. Dennis Jr. and R. B. Schnabel. *Numerical Methods for Unconstrained Optimization and Nonlinear Equations*. Prentice-Hall, Inc., 1983.

[16] Yangjun Luo, Ming Li, and Zhan Kang. Topology optimization of hyperelastic structures with frictionless contact supports. *International Journal of Solids and Structures*, 81:373–382, 3 2016.

[17] Michael A. Puso and Tod A. Laursen. A mortar segment-to-segment contact method for large deformation solid mechanics. *Computer Methods in Applied Mechanics and Engineering*, 193:601–629, 2 2004.

[18] L. Rakotondrainibe, G. Allaire, and P. Orval. Topology optimization of connections in mechanical systems. *Structural and Multidisciplinary Optimization*, 61:2253–2269, 6 2020.

[19] Lennart Scherz, Benedikt Kriegesmann, and Claus B. W. Pedersen. A condition number-based numerical stabilization method for geometrically nonlinear topology optimization. *International Journal for Numerical Methods in Engineering*, 8 2024.

[20] Timo Schmidt, Benedikt Kriegesmann, and Robert Seifried. Robust contact-constrained

topology optimization considering uncertainty at the contact support. *Structural and Multidisciplinary Optimization*, 67(4):46, apr 2024.

[21] Ole Sigmund. Morphology-based black and white filters for topology optimization. *Structural and Multidisciplinary Optimization*, 33:401–424, 2007.

[22] Antonio Signorini. Questioni di elasticità non linearizzata e semilinearizzata. *Rendiconti di Matematica e delle sue Applicazioni*, 5:95–139, 1959.

[23] Niclas Strömberg and Anders Klarbring. Topology optimization of structures in unilateral contact. *Structural and Multidisciplinary Optimization*, 41:57–64, 2010.

[24] Krister Svanberg. The method of moving asymptotes—a new method for structural optimization. *International Journal for Numerical Methods in Engineering*, 24:359–373, 2 1987.

[25] Simon Thomas, Qing Li, and Grant Steven. Topology optimization for periodic multicomponent structures with stiffness and frequency criteria. *Structural and Multidisciplinary Optimization*, 61:2271–2289, 6 2020.

[26] P Wriggers, · J Schröder, and · A Schwarz. A finite element method for contact using a third medium. 52:837–847, 2013.

[27] Peter Wriggers. *Computational Contact Mechanics*. Springer Berlin Heidelberg, Berlin, Heidelberg, 2006.